FUNDAMENTALS & APPLICATIONS

CHEMELECTROCHEM

ANALYSIS & CATALYSIS, BIO & NANO, ENERGY & MORE

Accepted Article

Title: New Carbon Monoliths for Supercapacitor Electrodes. Looking at the Double Layer.

Authors: Jose M Rojo, Gelines Moreno, Mirko Kunowsky, Maria Angeles Lillo-Rodenas, and Joaquin Ibañez

To be cited as: *ChemElectroChem* 10.1002/celc.201600848

Link to VoR: http://dx.doi.org/10.1002/celc.201600848

A Journal of

ChemPubSoc Europe

WILEY-VCH

www.chemelectrochem.org

10.1002/celc.201600848

Full paper

New Carbon Monoliths for Supercapacitor Electrodes. Looking at the Double Layer.

Gelines Moreno-Fernandez[1], *Mirko Kunowsky*[2], *Maria Ángeles Lillo-Ródenas*[2], *Joaquin Ibañez*[3] *and Jose M. Rojo*[1*]

[1]Instituto de Ciencia de Materiales de Madrid (ICMM); Consejo Superior de Investigaciones Científicas (CSIC); Sor Juana Inés de la Cruz, 3; Cantoblanco; E-28049-Madrid; Spain.

[2]MCMA Departamento de Química Inorgánica; Universidad de Alicante; San Vicente del Raspeig S/N; E-03080-Alicante; Spain.

[3]Centro Nacional de Investigaciones Metalúrgicas (CENIM); CSIC, Avda. Gregorio del Amo, 8; E-28040-Madrid; Spain.

*corresponding author: jmrojo@icmm.csic.es

Abstract

Carbon monoliths are prepared by combining two carbon phases. A major phase is activated anthracite, which provides microporosity and large surface area. The other phase is a carbonized polymer that provides self-consistency and contributes to densify the monolith. Different degrees of anthracite activation and different contents of the two phases are investigated. These all-carbon monoliths have surface areas up to 2600 $m^2 g^{-1}$, mechanical strengths up to 6 MPa, electrical conductivities up to 2-4 S cm^{-1} and densities between 0.4 and 0.7 g cm^{-3}. In sulfuric acid electrolyte, gravimetric capacitances up to 307 F g^{-1} are achieved. The double layer capacitances due to the hydronium and bisulfate ion are separately measured, the former being ca. 25 % higher than the latter. The size of the two ions electro-adsorbed at the double layer is discussed. The pseudocapacitance associated with the hydronium ion is 10-25% of the total capacitance of this ion. All the carbon monoliths show high capacitance retention on current density; the retention of the double layer capacitance is similar for the two types of ions and higher than the retention of the pseudocapacitance associated with the hydronium ion.

1. Introduction

Carbon monoliths are promising candidates for supercapacitor electrodes due to their three-dimensional framework of interconnected carbon particles that lead to high electrical conductivity and good accessibility of the electrolyte. The contact between adjacent particles in all-carbon monoliths is much better than that observed in pellets made from compaction under pressure of a powdered carbon and an inert polymer. In the latter case, the contact between the carbon particles is just of mechanical nature, while in the former case, the carbon particles are bonded by sintering. Accordingly, such all-carbon monoliths show much higher electrical conductivity (in the order of magnitude of 1 S cm^{-1}) than the compacted pellets (in the order of magnitude of 0.1 S cm^{-1}or lower).[1]

Another advantage of the carbon monoliths is their hierarchical porous structure, derived from the connectivity of macro (>50 nm), meso (2-50 nm) and micropores (< 2 nm), which can work as reservoirs and feeders of the electrolyte and provide a large double layer as a result of their large specific surface area.[2,3] All the carbon present in the monoliths can contribute to the capacitance. In contrast, the electrodes processed as compacted pellets of powdered carbon and polymeric binder can present isolated portions of the carbon, which are embedded in the binder and do not contribute to the capacitance.[1] The higher specific capacitance and the higher electrical conductivity of the monoliths compared to compacted pellets lead to supercapacitors with higher capacitance, lower resistance and shorter relaxation time.[1] The thickness of the monolith has an important effect on the supercapacitor features. As the monolith becomes thicker, (i) the cell capacitance increases significantly, which is an advantage, (ii) the cell resistance increases slightly, which is a moderate drawback, and (iii) the

relaxation time becomes longer, which is an important drawback. Thus, thicker monoliths are better for improving the cell energy and thinner monoliths are better for improving the cell power.[4,5] The main drawback of carbon monoliths is their low density, typically below 0.4 g cm^{-3}, that leads to low volumetric capacitances, usually below 100 $F \cdot cm^{-3}$ in aqueous electrolyte and below 50 $F \cdot cm^{-3}$ in organic electrolytes. There are only a few cases in which the reported monoliths showed densities above 1 g cm^{-3}. [6-8] In contrast, monolithic films prepared either from titanium carbides [9,10] or from graphene-like materials [11-16] showed densities up to 3.6 and 1.6 g cm^{-3}, respectively. These films reached volumetric capacitances as high as 800-900 $F \cdot cm^{-3}$ [9,15], but the volumetric capacitance, and also the specific (gravimetric) capacitance decreased as the film thickness increased, i.e. as the film became more compacted. [9,13,14,16] This feature is different from carbon monoliths, which showed the same gravimetric capacitance and the same density independently of the monolith thickness. [4]

Porous carbon monoliths can be prepared by a number of procedures and from different reagents: (i) carbonization of gels obtained from several carbon precursors and catalysts[17-28], (ii) carbonization of gels having a "soft template", which is thermally removed during carbonization, or a "hard template", subsequently removed by reaction with specific reagents after carbonization[29-36], (iii) infiltration of an inorganic monolith with a carbon precursor followed by carbonization and removal of the inorganic component [37-39], (iv) hydrothermal carbonization of biomass precursors[8,49,41], (v) carbonization of monoliths from natural biomaterials, such as pieces of wood, bone, etc. [42-44], and (vi) mold conforming under pressure of carbon or a carbon precursor followed by its carbonization.[45-47] The latter procedure is easier and cheaper than the others. However, the main difficulty comes from the fact that compaction of powdered

carbons does not lead to self-standing monoliths, but requires the use of a binder. Oftentimes, carbon monoliths prepared by the previously mentioned procedures reveal microporosity that comes from the carbon precursor, and macro/mesoporosity that is formed upon the removal of either the solvent or the template, leading to a hierarchical porosity.

In the present study, we report an easy and versatile procedure to obtain all-carbon monoliths that can be applied beyond the laboratory scale. The monoliths are made from two phases of porous carbon. The major phase is a powdered activated carbon obtained from anthracite activation. Anthracite can be easily activated in presence of alkaline hydroxides, such as potassium hydroxide.[48] This activated phase provides most of the porosity and specific surface area and, hence, a significant portion of the monolith capacitance. The other phase, which is a polymer-derived carbon, works as a scaffold and provides self-consistency. In this work, polyvinylidene chloride (PVDC) is chosen because, in contrast to other polymers, PVDC-derived carbons also provide a considerable amount of porosity,[49] which also contributes to the capacitance of the monoliths. Optimization of the monoliths in capacitance and self-consistency is accomplished by changing the activation degree of the former phase and the content of the latter one. A further aim of this work is to analyze the capacitance of the monoliths as a function of their content in the two carbon phases. Not only the total specific capacitance, which is usually studied, but also the specific capacitance associated with the two ions (cation and anion) of the electrolyte is analyzed, with the aim of discussing their contribution to the total specific capacitance. As far as we know, results of capacitance associated with the cation and anion are scarcely reported. However, this kind of results can help to get a better understanding of the double layer. The double layer capacitance and pseudo capacitance are discussed on the basis of the surface area

and surface chemistry of the monoliths. The size of the two ions electro-adsorbed at the double layer is also discussed.

2. Results and Discussion

Figure 1 shows SEM pictures of powdered anthracite before activation (top) and after KOH-activation with a KOH/anthracite weight ratio of 3/1 (bottom). The average particle size of the starting anthracite, of 500 µm, decreases after activation to an average value of 30 µm. While the starting anthracite has particles with a continuous and smooth appearance (inset of Figure 1a), the activated anthracite presents much rougher surfaces (inset of Figure 1b). Higher magnification (not shown) of the activated anthracite reveals smaller particles of carbon with sizes of 8-12 nm, similar to the particles observed for the AK31 activated anthracite phase (AA) in Figure 2c.

Figure 2 shows SEM pictures of the conformed MAK31 monolith before and after carbonization. It is important to underline that no monoliths can be obtained by compaction of the powdered activated anthracite phase without the presence of the carbonized PVDC binder phase.

Before carbonization, the backscattered electron (BSE) micrograph shows white, grey and black regions (Figure 2a). The white regions (B), which are ascribed to the PVDC, are located around the activated anthracite particles and around groups of these particles. The grey regions (AA) are ascribed to the activated anthracite particles. The black regions (V) are ascribed to voids. Larger voids, of 10-20 µm size, not filled with the PVDC, are observed between some neighboring anthracite particles. Smaller voids, of 1-2 µm size, are observed within some anthracite particles. Both the anthracite particles and the PVDC phase showed a high content of carbon, as deduced from EDS analysis. The PVDC phase also revealed a high content of chlorine (Figure S1).

After monolith carbonization (Figure 2b), the BSE micrograph shows: the carbonized PVDC phase (labeled CB), the activated anthracite particles (labeled AA) and the voids (labeled V). The CB phase is located around the AA particles and around groups of AA particles, and works as scaffold of the self-standing monolith. The two carbon phases, CB and AA, are in close contact, as observed from the magnified picture of the border between these phases (inset of Figure 2b). There are large voids of 10-20 µm in size between some adjacent AA particles and smaller voids of 1-2 µm in size within the CB phase and within some of the AA particles. The secondary electron (SE) micrographs of the two carbon phases show that they comprise connected carbon particles of smaller size (Figure 2c). The AA phase consists of carbon particles having 8-12 nm in size and voids of ca. 10 nm in size (left hand side of Figure 2c). These results suggest that the structure of the powdered activated anthracite was not modified after mold conforming and subsequent carbonization. The CB phase shows carbon particles of 15-30 nm in size and voids of 10-30 nm in size (right hand side of Figure 2c). Therefore, the two carbon phases consist of connected carbon particles and voids, both having sizes in the range 10-30 nm. The limit in resolution of the SEM technique prevents the detection of voids with sizes in the range of micropores, i.e., below 2 nm. The observed structure with interparticle voids in the range of 10-30 nm, 1-2 µm and 10-20 µm could be beneficial for the access of the electrolyte to the porosity of the monolith.

The N_2 adsorption isotherms of the four monoliths are shown in Figure 3a. The shapes of these isotherms correspond to type I, according to the IUPAC classification.[50] Thus, they show a sharp increase in the adsorbed nitrogen volumes at very low relative pressures (below 0.1 P/P_0) , whereas a plateau or only slight increase in the adsorbed volume in the mesoporous region (0.2-0.9 P/P_0) is observed. These two

features are characteristic of adsorbents with high microporosity[51]. The total adsorbed nitrogen volume, measured at P/P_0=0.99, increases as the KOH/anthracite ratio increases, i.e. from MAK11 to MAK21 and to MAK31. Therefore, the volume of nitrogen adsorbed by the carbon monoliths increases as the anthracite phase is progressively activated. Comparison of nitrogen adsorption isotherms for MAK31 and MAK31B reveals a lower porosity in the latter case. This is due to the higher content of carbonized binder in the MAK31B monolith, since the carbonized binder shows lower porosity than the activated anthracite phase (see Figure S3 and Table S1). The adsorption isotherms of the monoliths MAK11, MAK21 and MAK31 show a knee that becomes rounded as the anthracite phase is more activated, i.e. as the KOH/anthracite ratio increases from 1/1 to 2/1 and to 3/1. This feature indicates that the mean micropore size increases as the degree of the anthracite activation increases. Only a minor contribution of mesopores is found, slightly more noticeable in the case of the most activated monoliths. At relative pressures above 0.8-0.9 no further nitrogen adsorption can be observed, pointing out that the contribution of macroporosity to the total adsorbed volume is negligible. The pore size distributions (PSD) for the four monoliths, shown in Figure 3b, confirm that the sizes of most pores are below 2 nm, i.e. in the micropore size range, and that a widening of porosity occurs with increasing KOH/anthracite ratios.

Table 1 summarizes the physical-chemical properties of the four carbon monoliths. As expected, the largest specific BET surface area (close to 2600 m^2g^{-1}) and the highest total micropore volume (1 cm^3g^{-1}) are reached with monolith MAK31 for whose synthesis the highest KOH/anthracite ratio and the lowest amount of binder were used. The results in Table 1 confirm the qualitative observations made from Figure 3. Thus, the specific surface areas (S_{BET} and S_{DFT}), the mesopore volumes (V_{Meso}) and the

total micropore volumes ($V_{DR}(N_2)$) increase progressively from MAK11 to MAK21 and to MAK31, i.e. as the anthracite phase is progressively activated. Furthermore, the increase of the mean micropore size with increasing degree of activation is confirmed. Interestingly, a closer look to the micropores reveals that with the progress of the activation, the amount of narrow micropores (< 0.7 nm), i.e. $V_{DR}(CO_2)$, decreases, while the amount of wider micropores (between 0.7 and 2 nm), i.e. $V_{DR}(N_2)$-$V_{DR}(CO_2)$, increases. The mesopore volumes are relatively low for all of the monoliths (≤ 0.1 cm^3g^{-1}), confirming their essentially microporous character.

The rule of mixtures can be successfully applied to the specific surface areas of the three monoliths MAK11, MAK21 and MAK31. Hence, the experimental surface areas are in good agreement with the theoretical values, which are obtained by considering the percentages of the two phases in the final monoliths, as well as the surface areas of each activated anthracite and the carbonized binder (see Table S1). In contrast, the rule of mixtures does not give satisfactory results if applied to MAK31B, its experimental surface area being lower than the predicted one. This suggests that the larger micropores of the most activated anthracite (using KOH and a ratio of 3/1) can allow the entrance of the carbonized binder (15 wt. % vs. 8 wt. % used in MAK31), partially obstructing the anthracite pores. The fact that the rule of mixtures predicts well the surface area of the MAK11 monolith, also with binder content of 15 wt. %, but using a less activated anthracite (with a KOH/anthracite ratio of 1/1), suggests that the carbonized binder cannot enter into the narrow micropores of this activated anthracite.

Mechanical measurements by the three-point bending technique were carried out on the MAK21, MAK31 and MAK31B monoliths to understand the effects of the anthracite activation and the binder content on the strength of the monoliths. For the three monoliths, the stress increases as a function of the strain until attaining a

maximum value, the mechanical strength (Figure S2). This value is higher for MAK21 than for MAK31, and higher for MAK31B than for MAK31 (Table 2). Therefore, the strength of the monolith decreases as the anthracite is more activated, but increases as the content of carbonized binder increases.

The electrical conductivity of the four monoliths is in the range of 2-4 $S \cdot cm^{-1}$ (Table 2). Such values are comparable to those reported for other carbon monoliths [4-8] and higher than those reported for compacted pellets made from powder carbon and a polymeric binder.[1] This is an interesting feature of the carbon monoliths for their potential application as electrodes for supercapacitors.

The density of the carbon monoliths decreases from 0.70 to 0.38 g cm^{-3} as the anthracite phase is progressively activated (Table 2). A higher amount of carbonized binder leads to a higher density of the monolith, as deduced by comparing the densities of MAK31 and MAK31B. Consequently, MAK11, the monolith which was prepared from the less activated anthracite and a relatively high content of the carbonized binder, shows the highest density. Interestingly, the density of the investigated monoliths is higher than that of carbon monoliths typically obtained from a sol-gel procedure, usually below 0.4 g cm^{-3}.[2,3,18,20,28]

The surface chemistry of the monoliths was deduced with TPD by quantifying the evolved amounts of CO and CO_2, which originate from the oxygen groups at the surface of the carbon monoliths (Table 2). The highest amounts of CO and CO_2 were obtained for the MAK11 monolith, consisting of the less activated anthracite. As the anthracite phase was progressively activated, the contents of CO and CO_2 decrease, as deduced from comparison of monoliths MAK11, MAK21 and MAK31. The MAK31B monolith shows a similar amount of CO_2 but a higher amount of CO than the MAK31

monolith, both monoliths consisting of the same activated anthracite. This indicates that an important amount of CO is evolved from the carbonized binder. In accordance with this result, the highest amount of CO evolved from the MAK11 monolith results from the high content of the carbonized binder, in addition to the less activated anthracite.

In the literature, including a previous paper of some of the present authors, oftentimes SO_4^{2-} and H_3O^+ are reported as the dominant ions for the aqueous solution of sulfuric acid.[52] However, this is inaccurate due to the fact that the dissociation of sulfuric acid in water involves two stages. In the first stage, H_2SO_4 is completely transformed into HSO_4^- (bisulfate ion) and H_3O^+ (hydronium ion). In the second stage, the bisulfate ion is partially dissociated in SO_4^{2-} and H_3O^+, according to the equilibrium constant $Ka=10^{-1.99}$ at 25 ºC.[53] Then, the $[SO_4^{2-}]/[HSO_4^-]$ ratio is equal to 0.10 and the dominant ions are HSO_4^- and H_3O^+, which appeared in the first stage.

Figure 4 shows the galvanostatic charge/discharge plots recorded at 1 mA cm^{-2} (nearly steady state) for the monoliths MAK11 and MAK21 in presence of the sulfuric acid electrolyte. The thickness of these monoliths was ca. 2 mm. The open circuit potential (*OCP*) is different for the two monoliths, having a more positive value for the MAK11 monolith, the one with higher content in surface oxygen groups, as deduced from the higher contents of CO and CO_2. The plots show linear dependences (red straight lines) in the voltage range from -0.7 to 0.2 V; in this range, the total specific capacitance was determined according to $C_{total}=I\cdot t_d/\Delta V\cdot m$; where the parameters I, t_d, ΔV and m stand for the current applied, the time involved, the voltage range and the monolith weight, respectively. C_{total} is due to the contribution of both cations and anions, cations at negative voltages and anions at positive voltages. Below -0.7 V and above 0.2 V $E(t)$ departs from the straight line tending to a plateau; water decomposition happens evolving hydrogen and oxygen at voltages below -0.7 V and

above 0.2 V, respectively. The two decomposition voltages are labeled as E_d in Figure 4. The voltage ranges from the *OCP* to E_d on the side of positive voltages and negative ones are labeled as $\Delta V(HSO_4^-)$ and $\Delta V(H_3O^+)$, respectively.

Figure 5 shows the galvanostatic plots obtained for the MAK21 monolith at 1 mA cm^{-2} in the two voltage ranges, $\Delta V(HSO_4^-)$ and $\Delta V(H_3O^+)$. In this figure, "ads" and "des" stand for the electro-adsorption and electro-desorption of the two types of ions. The specific capacitance associated with the two types of ions was determined on the electro-desorption run to avoid possible interferences of the water decomposition with the capacitance measured. The specific capacitance associated with each ion was determined according to the equation $C(HSO_4^-)$ or $C(H_3O^+) = I \cdot t_d / \Delta V \cdot m$, where the parameters I, t_d, ΔV and m have the same meanings as already discussed. The specific capacitance measured for the bisulfate ion is ascribed to a double layer capacitance, i.e. $C(HSO_4^-)=C_{DL}(HSO_4^-)$; it agrees with the rectangular shape of its cyclic voltammetry (Figure S4). However, the specific capacitance measured for the hydronium ion shows a pseudo capacitance, $C_{PS}(H_3O^+)$, as deduced from the broad peak at ca. -0.2 V in the cyclic voltammetry (Figure S4), in addition to a double layer capacitance, $C_{DL}(H_3O^+)$. The pseudo capacitance is associated with reversible redox reactions happening over a broad potential range between the oxygen groups of the carbon and the hydronium ions of the electrolyte.[54,55] The double layer capacitance comes from the formation of the double layer between the electrolyte ions and the electrode charge at the electrolyte/electrode interface. Then, pseudocapacitance and double layer capacitance are independent from each other and the total capacitance $C(H_3O^+) = C_{PS}(H_3O^+) + C_{DL}(H_3O^+)$. Considering that $C_{DL}(H_3O^+)$ is proportional to the specific surface area and $C_{PS}(H_3O^+)$ is proportional to the amount of oxygen groups of the carbon that evolved as CO in TPD experiments, the values of those proportionality constants were estimated

for microporous carbons. The constant for the pseudo capacitance contribution is 0.042±0.008 F·μmolCO^{-1} in presence of the sulfuric acid electrolyte. [56] This constant is close, within experimental error, to the one reported by other authors.[57] Then, the pseudo capacitance for the four monoliths can be estimated according to:

$$C_{PS}(H_3O^+)=0.042\ \text{F}\ \mu\text{molCO}^{-1} \cdot \text{CO}\textit{content}\ (\mu\text{molCO}\ g^{-1}) \quad (1)$$

And the double layer capacitance $C_{DL}(H_3O^+)$ can be calculated according to:

$$C_{DL}(H_3O^+) = C(H_3O^+) - C_{PS}(H_3O^+) \quad (2)$$

Table 3 outlines the values of *OCP*, $\Delta V(HSO_4^-)$ and $\Delta V(H_3O^+)$, C_{total}, $C_{DL}(HSO_4^-)$, $C(H_3O^+)$, $C_{PS}(H_3O^+)$ and $C_{DL}(H_3O^+)$ for the four monoliths. The *OCP* value is slightly more positive for the MAK11 monolith than for the others, in accordance with its higher content of surface oxygen groups, i.e. the higher contents of CO and CO_2 deduced from TPD. The different value of the *OCP* for the MAK11 monolith makes $\Delta V(HSO_4^-)$ and $\Delta V(H_3O^+)$ different as compared to the other monoliths. Thus, $\Delta V(HSO_4^-)$ and $\Delta V(H_3O^+)$ show close values for the monoliths MAK21, MAK31 and MAK31B, but $\Delta V(H_3O^+) > \Delta V(HSO_4^-)$ for the MAK11 monolith. The C_{total} increases from the MAK11 monolith to the MAK21 one and to the MAK31 monolith. The value of C_{total} for MAK31B is close to that of MAK31; these values are as high as 307 and 304 Fg^{-1} for MAK31 and MAK31B, respectively. From galvanostatic measurements on symmetric two-electrode cells the capacitance of the cell, C_{2cell}, and the specific capacitance of each monolith, C_{2E}, were obtained (Figure S5). The values of the specific C_{total} are close to the values of specific C_{2E}. Thus, C_{total} values of 297, 307 and 304 F g^{-1} and C_{2E} values of 282, 290 and 288 F g^{-1} are obtained for the monoliths MAK21, MAK31 and MAK31B, respectively. The energy densities and power densities were calculated at each current on the basis of the mass of the two electrodes in the cell and are shown in a

characteristic Ragone plot in Figure S6. The energy density and power density reach maximum values of 9 Wh· kg^{-1} and 300 W·kg^{-1}, respectively, and were measured for the MAK31 monolith.

The values of C_{total} are the result of three contributions: the double layer capacitance of the anion, $C_{DL}(HSO_4^-)$, the double layer capacitance of the cation, $C_{DL}(H_3O^+)$, and the pseudo capacitance of the cation, $C_{PS}(H_3O^+)$. Comparing the three specific capacitances, $C_{DL}(H_3O^+)$ is slightly higher than $C_{DL}(HSO_4^-)$, and they are much higher than $C_{PS}(H_3O^+)$; therefore, the two former contribute much more than the latter and $C_{DL}(H_3O^+)$ contributes slightly more than $C_{DL}(HSO_4^-)$ to the value of C_{total}. The values of $C_{DL}(HSO_4^-)$ and $C_{DL}(H_3O^+)$ increase as the specific surface area increases, i.e. from MAK11 to MAK21 and to MAK31, and decrease as the specific surface area decreases, i.e. from MAK31 to MAK31B. The higher values of $C_{DL}(H_3O^+)$ compared to the ones of $C_{DL}(HSO_4^-)$, about 22-25 % higher, suggest larger available surface areas for the hydronium ion as compared with the bisulfate one. The values of $C_{PS}(H_3O^+)$ are proportional to the CO contents deduced from TPD; $C_{PS}(H_3O^+)$ decreases from MAK11 to MAK21 and to MAK31, but increases from MAK31 to MAK31B. The total volumetric capacitance obtained as $C_v=C_{total}\cdot d$ (where d is the monolith density) decreases from 167 F cm^{-3} for MAK11 to 154 F cm^{-3} for MAK21 and to 117 F cm^{-3} for MAK31. Despite C_{total} increases from MAK11 to MAK21 and to MAK31, the decrease in C_v points out the dominant effect of the density along the series. C_v value is higher for MAK31B than for MAK31, both monoliths having close values of C_{total} but the former showing a higher density. Although the volumetric capacitances of the four monoliths are rather high, they are lower than the values reported for highly densified carbon monoliths [6-8] and monolithic films. [9,13,14,16]

Table 4 compares the ratios of the double layer capacitances due to the hydronium and bisulfate ions, $C_{DL}(H_3O^+)/C_{DL}(HSO_4^-)$, with the ratios of the surface areas due to micropores with sizes above a certain value, $S_{>X}/S_{>Y}$. Thereby, the surface areas were estimated from the DFT data. For the four monoliths, the closest agreements with the $C_{DL}(H_3O^+)/C_{DL}(HSO_4^-)$ ratios are found for the $S_{>0.4}/S_{>0.5}$, the $S_{>0.4}/S_{>0.6}$ and the $S_{>0.5}/S_{>0.6}$ ratios; where $S_{>0.4}$, $S_{>0.5}$ and $S_{>0.6}$ are the surface areas due to micropores with sizes larger than 0.4, 0.5 and 0.6 nm, respectively. This suggests a minimum size of 0.4-0.5 nm for the hydronium ions and a minimum size of 0.5-0.6 nm for the bisulfate ions, as they are electro-adsorbed at the double layer. The size for the electro-adsorbed hydronium ion agrees with the partially hydrated $(H_3O)^+ \cdot nH_2O$ ion having n=1, i.e. the $H_5O_2^+$ ion.[58,59] The size for the electro-adsorbed bisulfate ion agrees with the size of the dehydrated ion[59-62] and also with the size reported for the electro-adsorbed sulfate ion.[63-65] For micropores with sizes above 0.6 nm, the electro-adsorbed bisulfate ion should appear as a hydrated ion. The hydration degree of both hydronium and bisulfate ion should increase as the pore size increases, as observed for the ions of KOH electrolyte in microporous carbons.[66]

From the specific surface areas estimated for pores with sizes larger than 0.4 nm ($S_{>0.4}$), 0.5 nm ($S_{>0.5}$ nm) and 0.6 nm ($S_{>0.6}$) on the one hand, and the double layer capacitances $C_{DL}(H_3O^+)$ and $C_{DL}(HSO_4^-)$ on the other, the double layer capacitance normalized by surface area results to be 0.22±0.04 F m^{-2} for both the hydronium ion and the bisulfate one. When the total S_{DFT} is considered, the normalized double layer capacitance is 0.15 and 0.12 F m^{-2} for the hydronium and bisulfate ion, respectively. The highest value of 0.22±0.04 F m^{-2} comes from the fact that the surface areas $S_{>0.4}$, $S_{>0.5}$ and $S_{>0.6}$ take values that are ca. 70, 63 and 55%, respectively, of the total S_{DFT} for the four monoliths. The value of 0.22±0.04 F m^{-2} is also higher than the value of

0.10±0.02 F m^{-2} deduced from the double layer capacitance measured in a two-electrode cell (due to the contribution of the two ions) and the total specific surface area.[56,57]

Finally, the dependence of the total specific capacitance, C_{total}, and the specific capacitance due to the hydronium ion, $C(H_3O^+)$, and bisulfate ion, $C(HSO_4^-)$, as a function of the current density are shown in Figure 6. C_{total} slightly decreases as the current density increases, showing high capacitance retention for the four monoliths (Figure 6a). The high capacitance retention agrees with the high electrical conductivity of the monoliths and the presence of voids (of meso and macroporous sizes) that favor mobility of the electrolyte within the monolith. For the MAK11 monolith, the capacitance retention has been analyzed separately for the hydronium and bisulfate ion. The extrapolation of $C(H_3O^+)$ as J→0 (see straight line in Figure 6b) gives a value of 183 F g^{-1}, which agrees with the value of 189 F g^{-1} deduced for $C_{DL}(H_3O^+)$ in Table 2. The difference between $C(H_3O^+)$ measured as J→0 and the value deduced from the extrapolated straight line at J→0 gives a value of 70 F g^{-1}, which is very close to the value of 64 F g^{-1} estimated for $C_{PS}(H_3O^+)$. Therefore, the decrease observed for $C(H_3O^+)$ in the range 0-25 mA·cm^{-2} can be ascribed to the pseudocapacitance of the hydronium ion. For current densities above 25 mA·cm^{-2}, the decrease of $C(H_3O^+)$ goes parallel to that of $C(HSO_4^-)$, the latter being ascribed to the double layer capacitance $C_{DL}(HSO_4^-)$. Then, above 25 mA·cm^{-2} the main contribution of $C(H_3O^+)$ is due to $C_{DL}(H_3O^+)$. The capacitance retention is better for $C_{DL}(H_3O^+)$ than for $C_{PS}(H_3O^+)$. Both $C_{DL}(H_3O^+)$ and $C_{DL}(HSO_4^-)$ depend on the current density in a similar way. This agrees with the fact that the hydronium and bisulfate ions are able to be electro-adsorbed at the double layer in micropores having a similar minimum size.

3. Conclusions

Carbon monoliths were prepared by a scalable two-step procedure. The monoliths consist of two carbon phases. The KOH-activated anthracite, which is the major phase, provides most of the porosity of the monolith. The oxygen content of this phase decreases as the activation progresses. The carbonized binder, placed around anthracite particles and groups of anthracite particles, provides self-consistency, mechanical strength and densification of the monolith, and also an additional content in porosity and surface oxygen groups. The SEM images confirmed a good contact between the two carbon phases and revealed a structure with voids that favors the access of the electrolyte to the monoliths' porosity. The monoliths are essentially microporous, reach BET surface areas up to 2600 m^2g^{-1} and show high electrical conductivity, between 2 and 4 S cm^{-1}.

The total specific capacitance mainly comes from the double layer capacitance due to the hydronium and bisulfate ions. The contribution of the former ion is around 25 % higher than that of the latter one. For the hydronium ion, the pseudo capacitance is 10-25 % of the total capacitance, i.e. the double layer capacitance plus the pseudo-capacitance. The minimum pore sizes in which the ions can be electro-adsorbed at the double layer are deduced to be 0.4-0.5 nm for the hydronium ion and 0.5-0.6 nm for the bisulfate ion. The former size is compatible with partially hydrated hydronium ions. The latter size agrees with the size of the dehydrated bisulfate ion. The double layer capacitance normalized by surface area results to be 0.22±0.04 F m^{-2} for the hydronium and the bisulfate ion, taking into account their double layer capacitances and the surface areas due to micropores with sizes above 0.4-0.5 and 0.5-0.6 nm, respectively.

The total capacitances (which reach more than 300 F g^{-1} at 1mA cm^{-2}) show a good retention on current density for all the monoliths. For the hydronium ion, the pseudo capacitance decreases more than the double layer capacitance as the current

density increases. The bisulfate ion only shows a double layer capacitance; its decrease on the current density is similar to the decrease observed for the double layer capacitance of the hydronium ion.

4. Experimental Section

The carbon monoliths were prepared by a two-step procedure. In the first step, powdered anthracite was activated in presence of KOH as activating agent. Anthracite and solid KOH were ground and mixed using KOH/anthracite weight ratios of 1/1, 2/1 and 3/1. Then, the mixtures were heated in a horizontal tube furnace under N_2 flow (500 ml min^{-1}) at a heating rate of 5ºC min^{-1} from room temperature to 700ºC. After holding this temperature for 1 h, the furnace was switched off and cooled down to room temperature in nitrogen. The products were extensively washed, first with 5M HCl solution and then with distilled water, and afterwards dried at 110ºC. Three different activated carbons were obtained, labeled AK11, AK21 and AK31, where A stands for anthracite, K for KOH-activation and the numbers stand for the KOH/anthracite weight ratio chosen for the activation.

No monoliths could be obtained by compaction of the powdered activated carbons without the addition of any other component. Thus, to prepare monoliths the activated anthracite was mixed with a 55 wt. % aqueous dispersion of PVDC (polyvinylidene chloride) (Waterlink Sutcliffe Carbons, UK). The mixtures were dried, ground, and compacted in a cylindrical mold at a pressure of 260 MPa. Subsequently, the mold with the compacted mixture was heated up to 140ºC. The conformed monoliths were carbonized in a horizontal tube furnace under a N_2 flow (100 ml min^{-1}) up to 750ºC. The heating protocol was performed using a constant heating rate of 1ºC min^{-1}, and holding three temperatures for different times: 175ºC was held for 1 h, 500ºC

was held for 1 h and, finally, 750ºC was held for 2 h. Then, room temperature was reached in nitrogen flow by switching off the furnace.

From the previous activated carbons (AK11, AK21 and AK31), four monoliths were prepared, which are labeled MAK11, MAK21, MAK31 and MAK31B, where M stands for "monolith", A for anthracite, K for KOH-activation and the numbers indicate the KOH/anthracite weight ratio. For the preparation of MAK21 and MAK31 monoliths, the content of carbonized PVDC in the final monoliths was relatively low (8 wt. %). Such amount of binder is sufficient for the cohesion of the monoliths and allows for the highest possible porosities. In the case of MAK11 and MAK31B, the content of carbonized PVDC was higher, 15 wt. %, in order to obtain monoliths with higher densities and volumetric capacitances. Hence, MAK31B consists of the same activated anthracite (AK31) as the MAK31 monolith, but with a higher content of the carbonized binder. A photograph of the as prepared MAK21 monolith is shown in Figure S7.

The microstructural characterization was performed by scanning electron microscopy (SEM) equipped with energy dispersive X-ray spectroscopy (EDS) in a FEG HITACHI S-4800 instrument. The carbon powders were supported on a conductive tape. The carbon monoliths were embedded in a resin and prepared by standard metallographic techniques. The images were obtained in the backscattered electron (BSE) mode or in the secondary electron (SE) mode. Analyses of the images were performed by using the Image-Pro Plus software.

Mechanical measurements were carried out by the three-point bending technique in a conventional 10T-SERVOSIS machine. The carbon monoliths had ca. 15 mm in length, 5 mm width and 2 mm thick. The span length, i.e. the distance between the two

supports, was 6.8 mm. The cross-head speed was 0.005 mm s^{-1}. Two tests were carried out for each monolith.

Temperature-programmed desorption (TPD) experiments were performed to characterize the surface chemistry of the monoliths by quantifying the evolved CO and CO_2 upon heating. The measurements were carried out in a TGA equipment (TA Instruments SDT Q600) which was coupled to a quadrupole mass spectrometer (Balzers Instruments Thermostar GSD 300 T3). Approximately 10 mg of sample were heated with a ramp of 10ºC min^{-1} up to 950ºC in a helium flow of 100 ml min^{-1}.

The density of the monoliths was deduced from their piece weight and volume, the former determined from the weight of the degassed samples and the latter from their geometric dimensions.

The electrical conductivity of parallelepipedic monoliths, ca. 6x6x2 mm^3, was determined by the four-probe method. A commercial silver paint was chosen to obtain the four probes.

N_2 adsorption/desorption isotherms at -196ºC were measured in a Micromeritics ASAP 2020. Prior to the adsorption, the monoliths were outgassed at 250ºC for 6 h.

The specific surface areas and the total micropore volumes were determined from the N_2 adsorption data. Thus, specific surface areas were deduced from Brunauer-Emmett-Teller theory (S_{BET}) and Non-Local Density Functional Theory (S_{DFT}). From the NLDFT, the pore size distribution (PSD) and the surface areas due to pores with sizes above a certain value were also deduced. Total volumes of micropores < 2 nm ($V_{DR}(N_2)$) and narrow micropores < 0.7 nm ($V_{DR}(CO_2)$) were calculated using Dubinin-Raduskevich. The total micropore volume was determined applying the Dubinin-Radushkevich equation to relative pressures below 0.1. The narrow micropore volumes

were determined applying the Dubinin-Radushkevich equation to the CO_2 adsorption isotherm in the 0.0144-0.0288 relative pressure range. The amount of mesopores was calculated from the small slope of the N_2 isotherm in the range from 0.2 to 0.9 relative pressures.[51]

For the electrochemical measurements, parallelepipedic monoliths having 25-50 mg in weight and ca. 2 mm in thickness were prepared. They were the working electrodes in three-electrode cells. Hg/Hg_2SO_4 and Pt wire were the reference and counter electrode, respectively. In some particular cases, symmetric two-electrode cells were assembled. The two equal monoliths were separated by a glassy microfiber paper (Whatman 934 AH). Aqueous 2M H_2SO_4 solution was used as electrolyte. Prior to the electrochemical measurements, the monoliths were immersed into the electrolyte and infiltrated under primary vacuum (ca. 10^{-1} Torr) for 2 days.

Supporting Information

Supporting Information is available from the Wiley Online Library

Acknowledgements

Prof. A. Linares-Solano, now retired, is deeply acknowledged for helpful discussions about preparation of carbon monoliths, activation and porosity. Financial support through the projects of reference MAT2014-57687-R, GV/FEDER (PROMETEOII/2014/010) and University of Alicante (VIGROB-136) is gratefully acknowledged. G. Moreno-Fernandez thanks MINECO for a pre-doctoral fellowship. Edurne Laurín is acknowledged for the preparation of SEM samples.

Keywords: carbon monoliths; EDLC; microporosity; sulfuric acid electrolyte; supercapacitors.

References

[1] A. Garcia-Gomez, P. Miles, T. A. Centeno, J. M. Rojo. *Electrohem. Solid-State Letters* **2010**, *13*, A112-A114.

[2] J. Biener, M. Stadermann, M. Suss, M. A. Worsley, M. M. Biener, K. A. Rose, T. F. Baumann. *Energy Environ. Sci.* **2011**, *4*, 656-667.

[3] S. L. Candelaria, R. Chen, Y.-H. Jeong, G. Cao. *Energy Environ. Sci.* **2012**, *5*, 5619-5637.

[4] A. Garcia-Gomez, P. Miles, T. A. Centeno, J. M. Rojo. *Electrochim. Acta* **2010**, *55*, 8539-8544.

[5] J. Chmiola, C. Largeot, P. L. Taberna, P. Simon, Y. Gogotsi. *Science* **2010**, *328*, 480-483.

[6] Y. Tao, X. Xie, W. Lv, D.-M. Tang, D. Kong, Z. Huang, H. Nishihara, T. Ishii, B. Li, D. Golberg, F. Kang, T. Kyotani, Q.-H Yang. *Sci. Rep.* **2013**, *3*, 2975.

[7] M. Kunowsky, A. Garcia-Gomez, V. Barranco, J. M. Rojo, J. Ibañez, J.D. Carruthers, A. Linares-Solano. *Carbon* **2014**, *68*, 553-562.

[8] C. Long, X. Chen, L. Jiang, L. Zhi, Z. Fan. *Nano Energy* **2015**, *12*, 141-151.

[9] M. Ghidiu, M. R. Lukatskaya, M.-Q. Zhao, Y. Gogotsi, M. W. Barsoum. *Nature* **2014**, *516*, 78-81.

[10] P. Huang, C. Lethien, S. Pinaud, K. Brousse, R. Laloo, V. Turq, M. Respaud, A. Demotiere, B. Daffos, P. L. Taberna, B. Chaudret, Y. Gogotsi, P. Simon. *Science* **2016**, *351*, 691-695.

[11] D. A. Dikin, S. Stankovich, E. J. Zimney, R. D. Piner, G. H. B. Dommett, G. Evmenenko, S. T. Nguyen, R. S. Ruoff. *Nature* **2007**, *448*, 457-460.

[12] X. Yang, J. Zhu, L. Qiu, D. Li. *Adv. Mater.* **2011**, *23*, 2833-2838.

[13] X. Yang, C. Cheng, Y. Wang, L. Qiu, D. Li. *Science* **2013**, *341*, 534-537.

[14] H. Li, Y. Tao, X. Zheng, Z. Li, D. Liu, Z. Xu, C. Luo, J. Luo, F. Kang, Q.-H. Yang. *Nanoscale* **2015**, *7*, 18459-18463.

[15] Y. Xu, Y. Tao, X. Zheng, H. Ma, J. Luo, F. Kang, Q.-H. Yang. *Adv. Mater.* **2015**, *27*, 8082-8087.

[16] H. Li, Y. Tao, X. Zheng, J. Luo, F. Kang, H.-M. Cheng, Q.-H. Yang. *Energy Environ. Sci.***2016**, *9*, 3135-3142.

[17] R.W. Pekala. *J. Mater. Sci.* **1989**, *24*, 3221-3227.

[18] R. Saliger, U. Fischer, C. Herta, J. Fricke. *J. Non-Cryst. Solids* **1998**, *225*, 81-85.

[19] C. Lin, J. A. Ritter, B. N. Popov. *J. Electrochem. Soc.* **1999**, *146*, 3639-3643.

[20] D. Wu, R. Fu, S. Zhang, M. S. Dresselhaus, G. Dresselhaus. *Carbon* **2004**, *42*, 2033-2039.

[21] B. Fang, Y.-Z. Maruyama, M. Kumagai. *J. Appl. Electrochem.* **2005**, *35*, 229-233.

[22] N. Tonanon, A. Siyasukh, Y. Wareenin, T. Charinpanitkul, V. Tanthapanichakoon, H. Nishihara, S. R. Mukai, H. Tamon. *Carbon* **2005**, *43*, 2808-2811.

[23] S. J. Kim, S. W. Hwang, S. H. Hyun. *J. Mater Sci.* **2005**, *40*, 725-731.

[24] J. Li, X. Wang, Q. Huang, S. Gamboa, P. J. Sebastian. *J. Power Sources* **2006**, *158*, 784-788.

[25] D. Tashima, M. Taniguchi, D. Fujikawa, T. Kijima, M. Otsubo. *Mater. Chem. Phys.* **2009**, *115*, 69-73.

[26] A. Halama, B. Szubzda, G. Pasciak. *Electrochim. Acta* **2010**, *55*, 7501-7505.

[27] E. G. Calvo, C. O. Ania, L. Zubizarreta, J. A. Menendez, A. Arenillas. *Energy Fuels* **2010**, *24*, 3334-3339.

[28] M. Zeller, V. Lorrmann, G. Reichenauer, M. Wiener, J. Pflaum. *Adv. Energy Mater.* **2012**, *2*, 598-605.

[29] D. Carriazo, F. Pico, M. C. Gutierrez, F. Rubio, J. M. Rojo, F. del Monte. *J. Mater. Chem.* **2010**, *20*, 773-780.

[30] N. Brun, S. R. S. Prabaharan, C. Surcin, M. Morcrette, H. Deleuze, M. Birot, O. Babot, M.-F. Achard, R. Backov. *J. Phys. Chem. C* **2011**, *116*, 1408-1421.

[31] T. F. Baumann, J. H. Satcher Jr. *J. Non-Cryst. Solids* **2004**, *350*, 120-125.

[32] P. X. Hou, H. Orikasa, H. Itoi, H. Nishihara, T. Kyotani. *Carbon* **2007**, *45*, 2011-2016.

[33] D.-W. Wang, F. Li, M. Liu, G. Q. Lu, H.-M. Cheng. *Angew. Chem. Int. Ed.* **2008**, *47*, 373-376.

[34] M. M. Bruno, N. G. Cotella, M. C. Miras, C. A. Barbero. *Colloids and Surfaces A: Physicochem. Eng. Aspects* **2010**, *362*, 28-32.

[35] G. Hasegawa, K. Kanamori, K. Nakanishi, T. Abe. *J. Phys. Chem. C* **2012**, *116*, 26197-26203.

[36] M. Sevilla, A. B. Fuertes. *Carbon* **2013**, *56*, 155-166.

[37] H. Yang, Q. Shi, X. liu, S. Xie, D. Jiang, F. Zhang, C. Yu, Bo Tu, D. Zhao. *Chem Commun.* **2002**, 2842-2843.

[38] A. Taguchi, J.-H. Smatt, M. Linden. *Adv. Mater.* **2003**, *15*, 1209-1211.

[39] Z.-G. Shi, Y.-Q Feng, L. Xu, S.-L. Da. *Carbon* **2003**, *41*, 2668-2670.

[40] T.-P. Fellinger, R. J. White, M. M. Titirici, M. Antonietti. *Adv. Funct. Mater.* **2012**, *22*, 3254-3260.

[41] Y. Gong, Z. Wei, J. Wang, P. Zhang, H. Li, Y. Wang. *Sci. Rep.* **2014**, *4*, 6349.

[42] P. A. Goodman, H. Li, Y. Gao, Y. F. Lu, J. D. Stenger-Smith, J. Redepenning. *Carbon* **2013**, *55*, 291-298.

[43] M. C. Liu, L.-B. Kong, P. Zhang, Y.-C. Luo, L. Kang. *Electrochim. Acta* **2012**, *60*, 443-448.

[44] A. Cuña, N. Tancredi, J. Bussi, V. Barranco, T. A. Centeno, A. Quevedo, J. M. Rojo. *J. Electrochem. Soc.* **2014**, *161*, A1806-A1811.

[45] D. Lozano-Castello, D. Cazorla-Amoros, A. Linares-Solano, D. F. Quinn. *Carbon* **2002**, *40*, 2817-2825.

[46] V. Ruiz, C. Blanco, R. Santamaria, J. M. Ramos-Fernandez, M. Martinez-Escandell, A. Sepulveda-Escribano, F. Rodriguez-Reinoso. *Carbon* **2009**, *47*, 195-200.

[47] E. Taer, M. Deraman, I. A. Talib, A. Awitdrus, S. A. Hashmi, A. A. Umar. *Int. J. Electrochem. Sci.* **2011**, *6*, 3301-3315.

[48] D. Lozano-Castello, M. A. Lillo-Rodenas, D. Cazorla-Amoros and A. Linares-Solano. *Carbon* **2001**, *39*, 741-749.

[49] M. Endo, Y. J. Kim, T. Takeda, T. Maeda, T. Hayashi, K. Koshiba, H. Hara, M. S. Dresselhaus. *J. Electrochem. Soc.* **2001**, *148*, A1135-A1140.

[50] M. Thommes, K. Kaneko, A. V. Neimark, J. P. Olivier, F. Rodriguez-Reinoso, J. Rouquerol, K. S. W. Sing. Physisorption of gases, with special reference to the evaluation of surface area and pore size distribution (IUPAC Technical Report), *Pure Appl. Chem.* **2015**, *87*, 1051–1069.

[51] Microporous Structure of Activated Carbons as Revealed by Adsorption Methods, F. Rodriguez-Reinoso, A. Linares-Solano. Chemistry and Physics of Carbon. Volume 21, pages 1-146, year 1988". Ed. P. A. Thrower, Editorial Marcel Dekker, New York.

[52] V. Barranco, A. Garcia-Gomez, M. Kunowsky, A. Linares-Solano, J. Ibañez, M. King, J. M. Rojo. *J. Power Sources* **2014**, *262*, 23-28.

[53] Handbook of Chemistry and Physics. 88th Edition. D.R. Lide editor. 2007-2008. Page 8-41.

[54] C. T. Hsieh, H. Teng. *Carbon* **2002**, *40*, 667-674.

[55] E. Raymundo-Piñero, F. Leroux, F. Beguin. *Adv. Mater.* **2006**, *18*, 1877-1882.

[56] V. Barranco, M. A. Lillo-Rodenas, A. Linares-Solano, A. Oya, F. Pico, J. Ibañez, F. Agullo-Rueda, J. M. Amarilla, J. M. Rojo. *J. Phys. Chem. C* **2010**, *114*, 10302-10307.

[57] T. A. Centeno, M. Hahn, J. A. Fernandez, R. Kotz, F. Stoeckli. *Electrochem. Commun.* **2007**, *9*, 1242-1246.

[58] R. Mancinelli, A. Sodo, F. Bruni, M. A. Ricci, A. K. Soper. *J. Phys. Chem. B* **2009**, *113*, 4075-4081.

[59] T. Ishiyama, A. Morita. *J. Phys. Chem. C* **2011**, *115*, 13704-13716.

[60] V. Vchirawongkwin, C. Kritayakornupong, B. M. Rode. *J. Phys. Chem. B* **2010**, *114*, 11561-11569.

[61] J.-J. Yu, Y.-H. Zhang, Z.-S. Li. *J. Phys. Chem. B* **2012**, *116*, 12597-12604.

[62] D. E. Husar, B. Temelso, A. L. Ashworth, G. C. Shields. *J. Phys. Chem. A* **2012**, *116*, 5151-5163.

[63] L. Eliad, G. Salitra, A. Soffer, D. Aurbach. *J. Phys. Chem. B* **2001**, *105*, 6880-6887.

[64] L. Eliad, G. Salitra, A. Soffer, D. Aurbach. *J. Phys. Chem. B* **2002**, *106*, 10128-10134.

[65] V. Ruiz, C. Blanco, R. Santamaria, J. M. Juarez-Galan, A. Sepulveda-Escribano, F. Rodriguez-Reinoso. *Micro. Mesopore Mater.* **2008**, *110*, 431-435.

[66] A. Garcia-Gomez, V. Barranco, G. Moreno-Fernandez, J. Ibañez, T. A. Centeno, J. M. Rojo. *J. Phys. Chem. C* **2014**, *118*, 5134-5141.

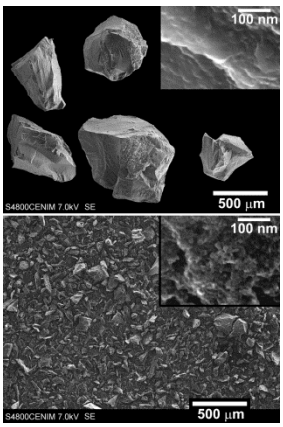

Figure 1. SEM pictures of the powdered starting anthracite (top) and the activated AK31 anthracite (bottom). The insets show magnified pictures of the two samples.

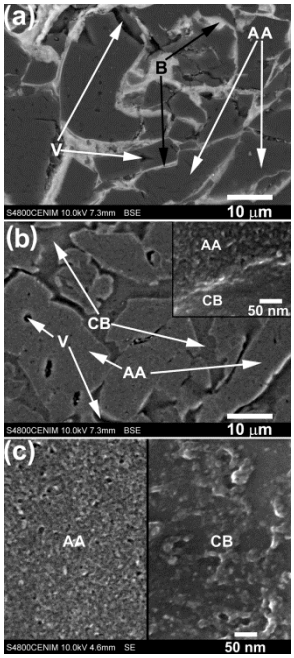

Figure 2. SEM pictures for the conformed MAK31 monolith before and after carbonization: (a) the mold conforming monolith having powder of the AK31 activated anthracite (AA), aqueous dispersion of the polymeric binder (B) and some voids (V); (b) the same monolith after carbonization showing the AK31 activated anthracite (AA), the carbonized binder (CB) and some voids (V); the inset shows a magnification of the border between the two carbon phases; (c) magnification of the two carbon phases, AA and CB. Images in (a) and (b) were obtained by the BSE mode. Images in (c) were obtained by the SE mode.

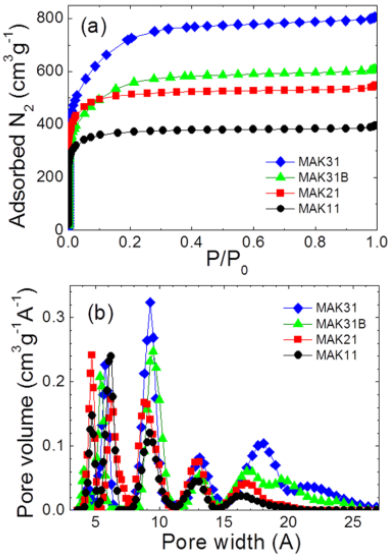

Figure 3. (a) Nitrogen adsorption isotherms at -196ºC of the four carbon monoliths. (b) DFT pore size distributions of the four monoliths.

10.1002/celc.201600848

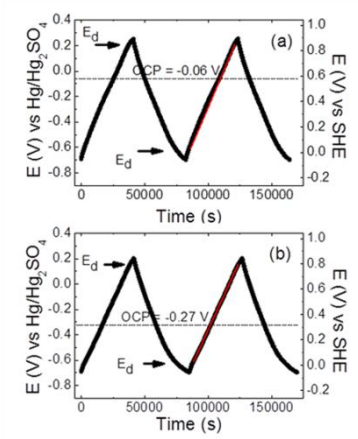

Figure 4. Galvanostatic plots obtained at 1 mA cm^{-2} on the MAK11 (a) and the MAK21 monoliths (b). E_d stands for the decomposition voltage. The measurements were carried out in the total voltage range of 0.90 V. Aqueous 2M H_2SO_4 solution was the electrolyte.

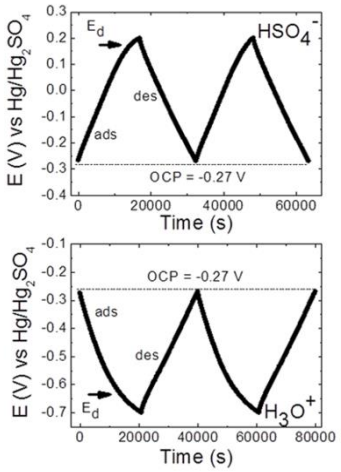

Figure 5. Galvanostatic plots obtained for the bisulfate ion (top) and hydronium ion (bottom) at 1 mA cm^{-2}. The carbon monolith was MAK21. E_d stands for the decomposition voltage. "ads" and "des" stand for the electro-adsorption and electro-desorption of the ions, respectively.

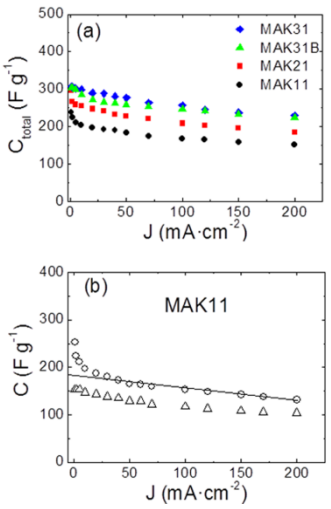

Figure 6. (a) Total specific capacitance vs. current density for the four monoliths. (b) Specific capacitance due to the hydronium ion (circles) and bisulfate ion (triangles) vs. current density for the MAK11 monolith.

Table 1. Characteristics of the four carbon monoliths. KOH/anthracite weight ratio, carbonized PVDC content, specific surface areas (S_{BET} and S_{DFT}), mesoporous volume (V_{Meso}), total micropore volume ($V_{DR,N2}$), narrow micropore volume ($V_{DR,CO2}$) and the difference between these volumes ($V_{DR,N2}$-$V_{DR,CO2}$).

Monolith	KOH/ anthracite	PVDC (wt.%)	S_{BET} (m^2g^{-1})	S_{DFT} (m^2g^{-1})	V_{Meso} (cm^3g^{-1})	$V_{DR,N2}$ (cm^3g^{-1})	$V_{DR,CO2}$ (cm^3g^{-1})	$V_{DR,N2}$-$V_{DR,CO2}$ (cm^3g^{-1})
MAK11	1/1	15	1287	1491	0.019	0.57	0.52	0.05
MAK21	2/1	8	1798	1947	0.030	0.75	0.48	0.27
MAK31	3/1	8	2583	2117	0.101	1.01	0.42	0.59
MAK31B	3/1	15	1968	1707	0.061	0.71	0.37	0.34

Table 2. Maximum stress (σ_M), electrical conductivity (σ), piece density (d), contents of CO and CO_2 from TPD for the four carbon monoliths.

Monolith	σ_M (MPa)	σ (Scm^{-1})	d (gcm^{-3})	CO ($\mu molg^{-1}$)	CO_2 ($\mu molg^{-1}$)
MAK11	--	3	0.70	1514	569
MAK21	5.3	4	0.52	982	395
MAK31	1.9	2	0.38	685	378
MAK31B	6.1	3	0.44	1028	378

Table 3. Open circuit potential (*OCP*) vs. Hg/Hg_2SO_4, voltage range from the *OCP* to the electrolyte decomposition voltage for positive voltages (ΔV (HSO_4^-)) and negative ones (ΔV (H_3O^+)), total specific capacitance (C_{total}) due to the contribution of the anion and cation, and specific capacitance due to the anion ($C(HSO_4^-)$) and cation ($C(H_3O^+)$). The estimated pseudocapacitance ($C_{PS}(H_3O^+)$) and double layer capacitance ($C_{DL}(H_3O^+)$) for the hydronium ion and the double layer capacitance for the bisulfate ion ($C_{DL}(HSO_4^-)$). The total volumetric capacitance (*Cv*) is also shown.

Monolith	*OCP* (V)	$\Delta V(HSO_4^-)$ (V)	$\Delta V(H_3O^+)$ (V)	C_{total} (Fg^{-1})	$C_{DL}(HSO_4^-)$ (Fg^{-1})	$C(H_3O^+)$ (Fg^{-1})	$C_{PS}(H_3O^+)$ (Fg^{-1})	$C_{DL}(H_3O^+)$ (Fg^{-1})	(
MAK11	-0.06	0.31	0.64	238	153	253	64	189	
MAK21	-0.27	0.47	0.43	297	270	371	41	330	
MAK31	-0.29	0.49	0.41	307	282	374	29	345	
MAK31B	-0.28	0.48	0.42	304	258	365	43	322	

Table 4. Ratios of the double layer capacitances due to hydronium ion and bisulfate one and ratios of the surface areas due to micropores with sizes higher than a certain value (expressed in nm).

Monolith	$C_{DL}(H_3O^+)$/ $C_{DL}(HSO_4^-)$	$S_{>0.4}$ / $S_{>0.5}$	$S_{>0.4}$ / $S_{>0.6}$	$S_{>0.4}$ / $S_{>0.7}$	$S_{>0.4}$ / $S_{>0.9}$	$S_{>0.5}$ / $S_{>0.6}$	$S_{>0.5}$ / $S_{>0.7}$	$S_{>0.5}$ / $S_{>0.9}$
MAK11	1.24	1.27	1.66	2.63	3.43	1.30	2.07	2.70
MAK21	1.22	1.39	1.52	2.07	3.14	1.09	1.49	2.26
MAK31	1.22	1.05	1.35	1.39	1.73	1.29	1.33	1.65
MAK31B	1.25	1.07	1.44	1.44	1.59	1.34	1.34	1.48

10.1002/celc.201600848

Table of contents

The work deals with preparation and electrochemical response of new carbon monoliths as electrodes for supercapacitors. The monoliths consist of an activated carbon that provides porosity and a carbonized binder that provides self-consistency. The specific capacitance is analyzed on the basis of the monolith composition and compared with that associated with the electrolyte cation and anion. The capacitance retention on current density is also studied.